Supplementary Materials for

Spin-Constraint Optoelectronic Functionality in Two-Dimensional Ferromagnetic Semiconductor Heterojunctions

Yilv Guo,[a†] Yehui Zhang,[a†] Zhaobo Zhou,[a] Xiwen Zhang,[b] Bing Wang,[c] Shijun Yuan,*[a] Shuai Dong[a] and Jinlan Wang*[a]

[a] School of Physics, Southeast University, Nanjing 211189, China
[b] School of Mechanism Engineering & School of Physics, Southeast University, Nanjing 211189, China
[c] Institute for Computational Materials Science, School of Physics and Electronics, Henan University, Kaifeng 475004, China

[†]These authors contributed equally.
*E-mail: siesta@seu.edu.cn; jlwang@seu.edu.cn

Table S1. **Variations of band-gap types of bilayer FMSs with the change in the external magnetic field.** From P to AP, the spin-up and spin-down channels are taken into account.

Gap-type	Band alignment			
up	Type I → Type I	Type I → Type II	Type II → Type I	Type II → Type II
dn	Type I → Type I	Type I → Type II	Type II → Type I	Type II→ Type II

Table S2. **Physical properties of monolayer CrX_3.** Lattice constant (a) of unit cell, ferromagnetic (FM) and Néel antiferromgnetic (Néel-AFM) energy, magnetic anisotropy energies (MAE, energy difference between in-plane and out-of-plane magnetic anisotropic energy), the nearest magnetic exchange coupling (J_1) of CrX_3 monolayers.

	a (Å)	FM (meV/f.u.)	Néel-AFM (meV/f.u.)	MAE (ueV/f.u.)	J_1 (meV)
CrF_3	5.208	0	17.0	62	1.265
$CrCl_3$	6.051	0	31.5	14	2.384
$CrBr_3$	6.417	0	41.0	129	3.088
CrI_3	6.970	0	52.3	740	3.888

Table S3. Validation of k-point mesh. k-point mesh, total energy of AP and P states, respectively, energy difference between AP and P state.

K-points	E_{AP} (eV/unit cell)	E_P (eV/unit cell)	E_{AP-P} (meV/unit cell)
2	-69.846871	-69.849593	2.72
3	-69.890489	-69.893108	2.62
4	-69.890489	-69.893092	2.60
5	-69.890451	-69.893054	2.60
6	-69.890408	-69.893012	2.60
7	-69.890455	-69.893059	2.60
8	-69.89042	-69.893024	2.60
9	-69.890405	-69.893009	2.60

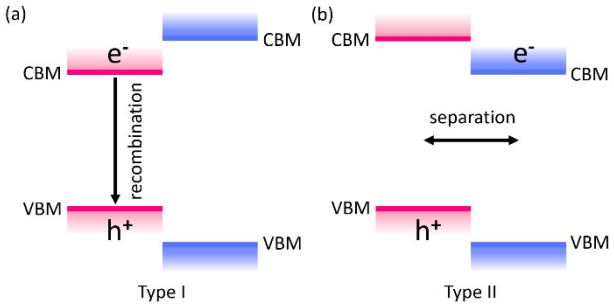

Figure S1. Illustration of (a) type-I and (b) type-II band alignment configurations for vdW heterostructure.

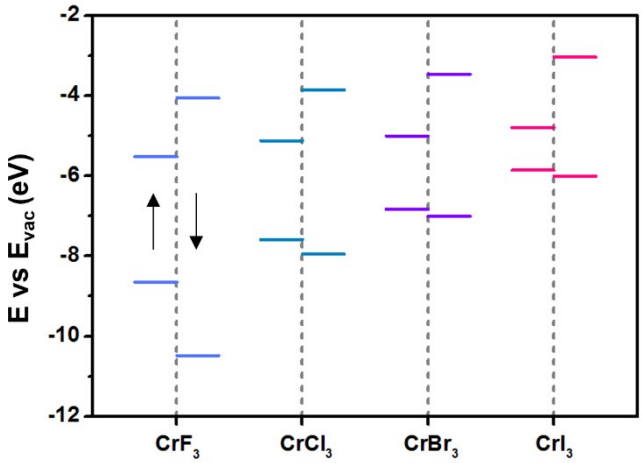

Figure S2. Calculated spin-polarized band edges. Comparatively spin-polarized band alignment of CrX_3 with respect to vacuum level. Up and down arrows represent spin-up and spin-down channels.

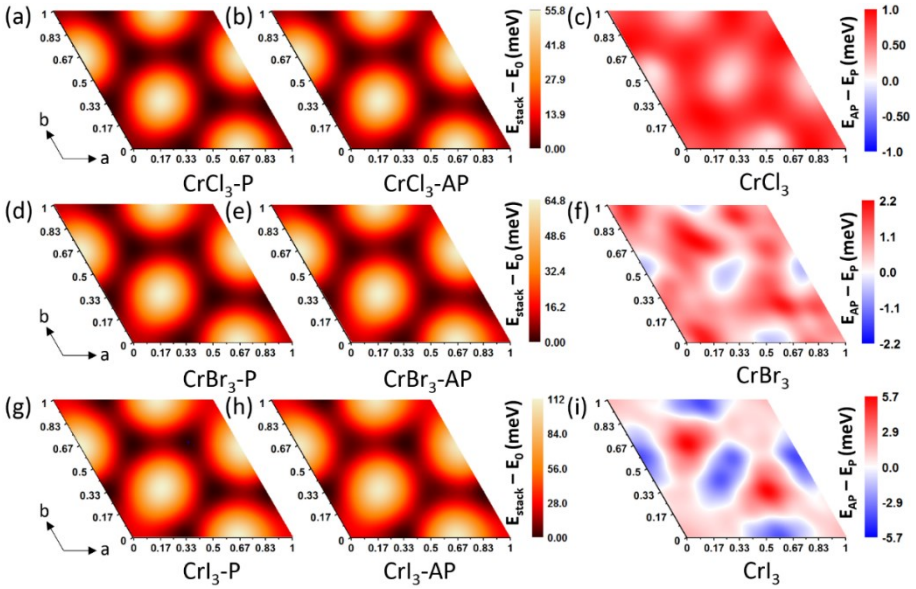

Figure S3. Relative stacking energy for P and AP states according to lateral shift, and the corresponding energy difference between AP and P states. (a-c) correspond to bilayer $CrCl_3$, (d-f) correspond to bilayer $CrBr_3$ and (g-i) correspond to bilayerCrI_3.

The employed DFT method was carefully justified in our work, which well reproduces the available experimental results. The current methodology predicted that the Curie temperature (T_c) of CrI_3 monolayer is 43 K[2], in good line with the measured value of 45 K[1]. Moreover, experiments show that the interlayer antiferromagnetic and ferromagnetic behaviors of bilayer CrI_3 are determined by the monoclinic and rhombohedral phases, respectively.[3-5] Our results (Figure S3) show that the relative energies of bilayer CrI_3 in P and AP states are strongly dependent on stacking orders as well, consistent with above experimental results.

From X = I to Cl, the stacking energies (E_{AP} - E_P) of CrX_3 show a hexagonal pattern, while the weak P state gradually dominates the global ground state. Such changes are related to the size, electronegativity, spin-orbital coupling strength of halogen elements, and the intensity of covalency for Cr-halogen bonds in CrX_3.[6]

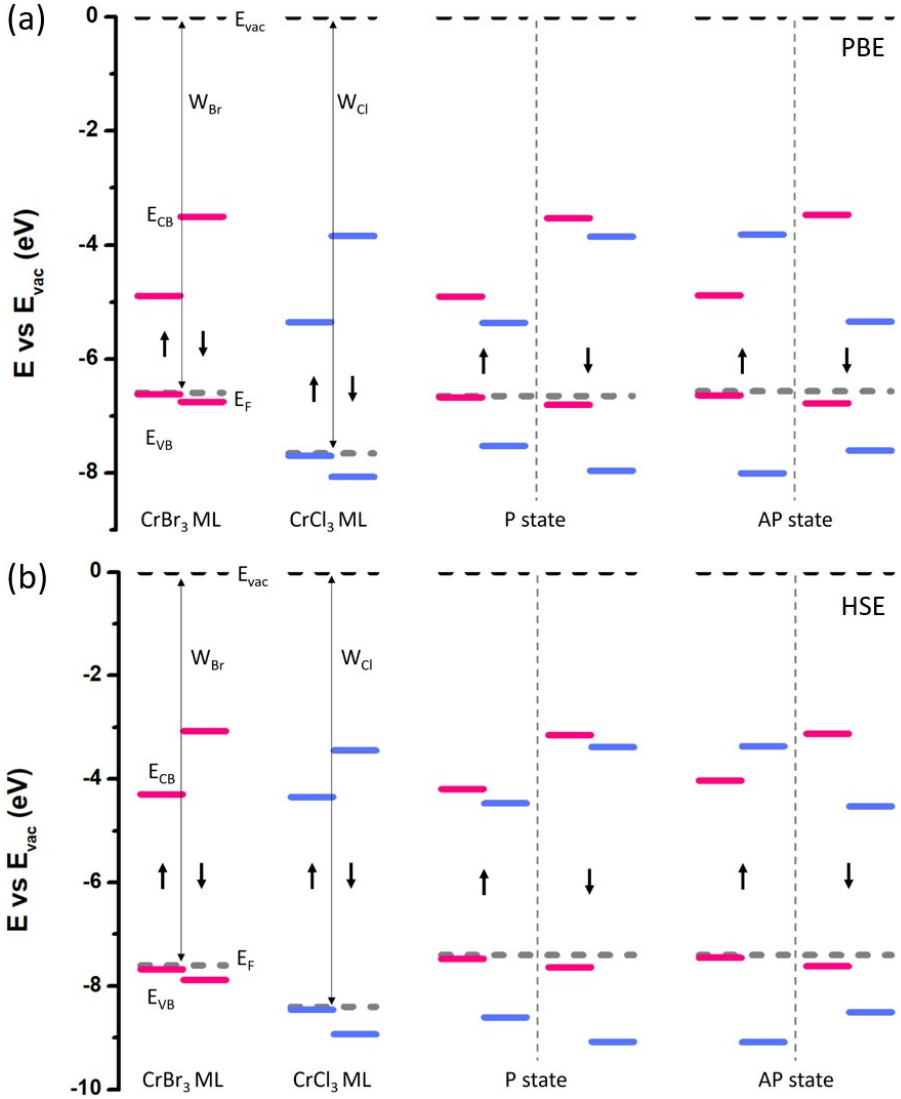

Figure S4. Comparations of the band-edge energy levels for the isolated $CrBr_3$, $CrCl_3$ monolayers and $CrBr_3$/$CrCl_3$ heterostructure with respect to the vacuum at (a) PBE and (b) HSE levels, respectively. W_{Cl} and W_{Br} represent the work function of $CrCl_3$ and $CrBr_3$, respectively. E_{CB}, E_{VB} and E_F represent CBM, VBM and Fermi level, respectively. Black up and down arrows represent spin-up and spin-down channels, respectively.

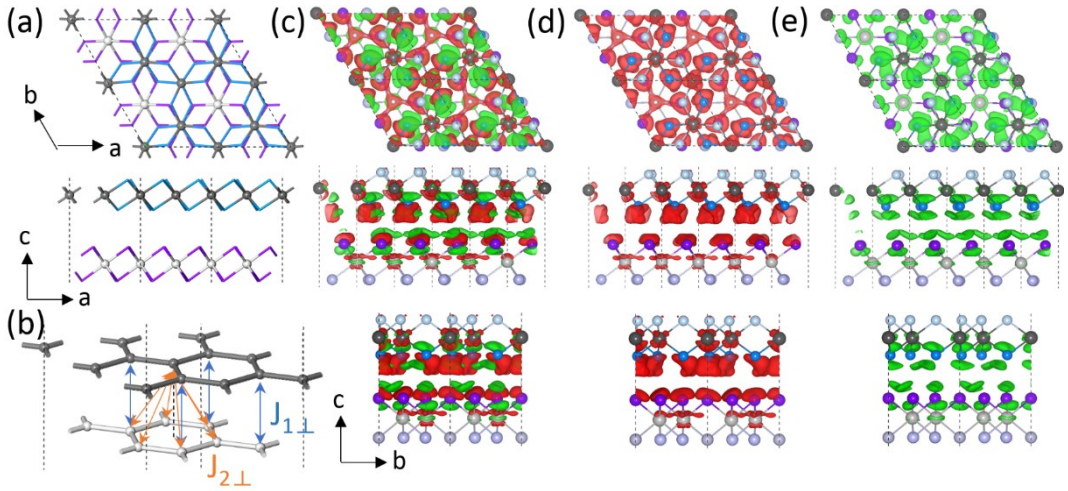

Figure S5. **Differential charge densities for AB stacking.** (a) Top view and side view of AB-stacking $CrBr_3/CrCl_3$ heterostructure, and (b) Corresponding interlayer nearest and next-nearest neighboring exchange interaction, labeled as J_1 and J_2, respectively. (c) Differential charge density, and charge (d) accumulation (red) and (e) depletion (green) density are plotted separately. The isosurface value is set as 0.00004 e/Å^3.

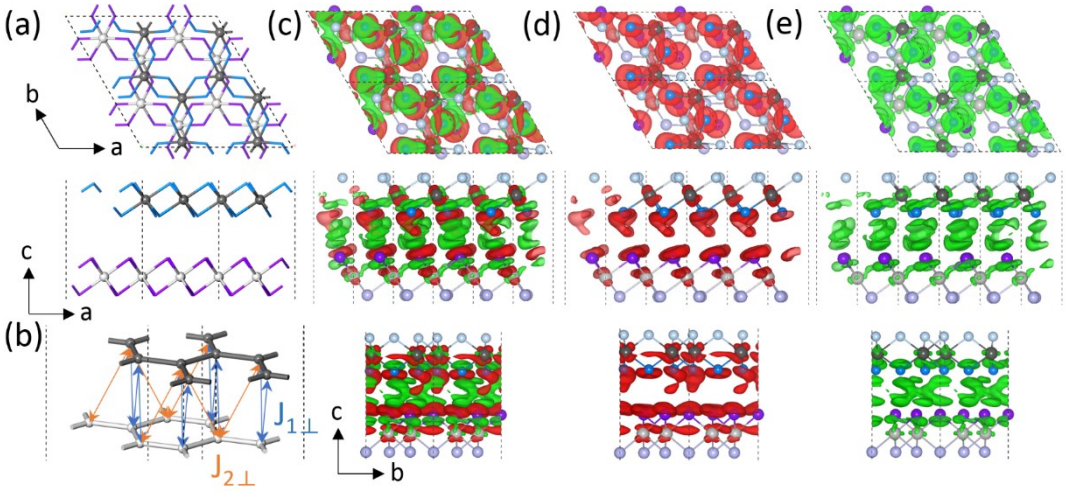

Figure S6. **Differential charge densities for AC stacking.** (a) Top view and side view of AC-stacking $CrBr_3/CrCl_3$ heterostructure, and (b) Corresponding J_1 and J_2, respectively. (c) Differential charge density, and the charge (d) accumulation (red) and (e) depletion (green) density are plotted separately. The isosurface value is set as 0.00004 e/Å^3.

To explore the interlayer coupling, structures of AB- and AC-stacking and differential charge densities for P and AP states are compared in Figure S5 and S6. Different magnetic interlayer exchange terms are first considered. There are one nearest neighboring exchange term and six next-nearest exchange terms for each Cr atom in AB-stacking (FigureS5a and S5b), while two nearest neighboring exchange terms and two next-nearest terms for AC-stacking (Figure S6a and S6b). The differential charge densities in P-state AB-stacking (Figure S5c-e) and AP-state AC-stacking (Figure S6c-e) are further compared, and obviously distinct interlayer charge redistributions are found. The accumulated spin-up and spin-down charge densities are found on

halogen atoms at the interlayer surface for AB-stacking. While a partial overlap of the spin-down densities is observed between $CrBr_3$ and $CrCl_3$ layers in AC-stacking.

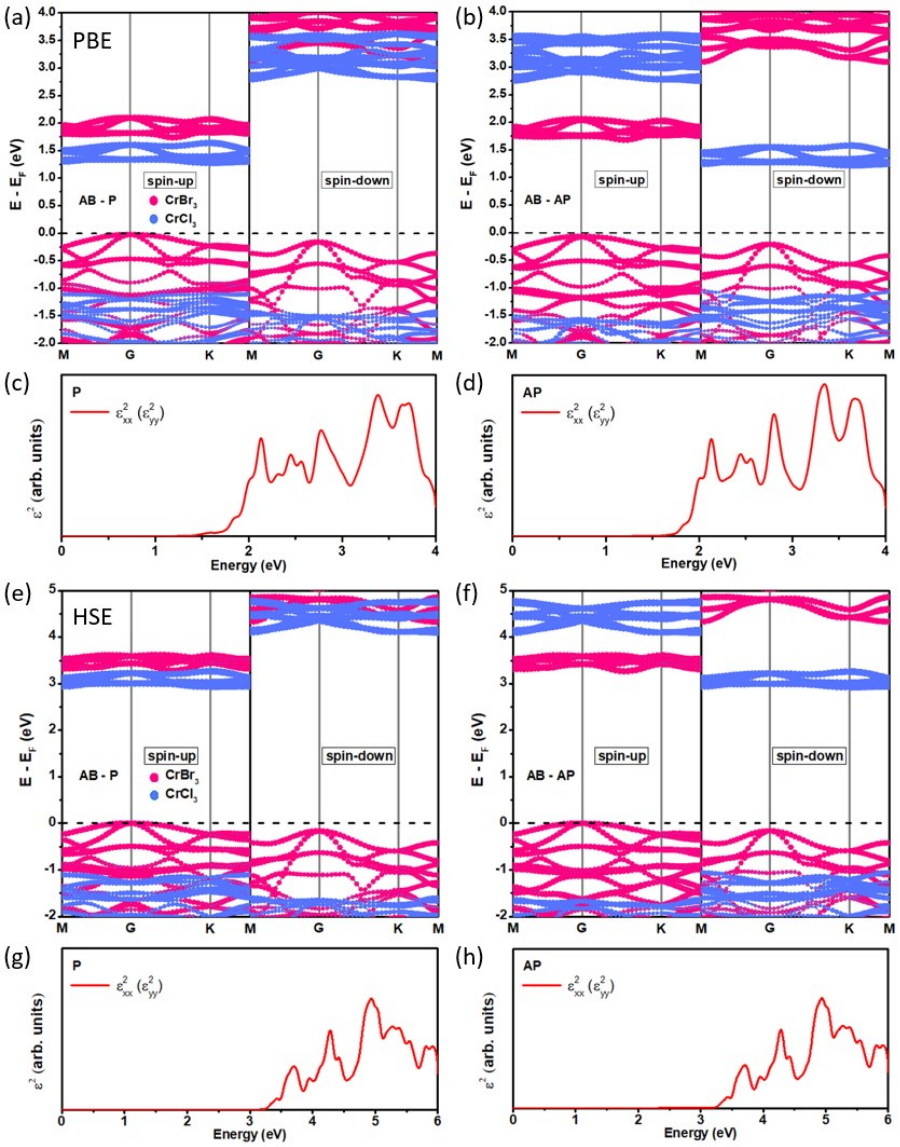

Figure S7. Comparations of the band structures and optical properties for $CrBr_3/CrCl_3$ heterostructure at PBE and HSE levels, respectively. Calculated (a and b) band structures and (c and d) imaginary part of the dielectric constant of $CrBr_3/CrCl_3$ heterostructure using PBE for P and AP states in AB stacking, respectively. (e and f) Band structures and (g and h) imaginary part of the dielectric constant of $CrBr_3/CrCl_3$ heterostructure using HSE for P and AP states in AB stacking, respectively. Fermi level is set to 0.

It is known that the PBE calculations often underestimates the bandgap of semiconductors. To obtain more accurate band structures, Hybrid HSE06 method was further employed. As shown in Figure S7, the band shapes at PBE level (Figure S7a and S7b) are similar with those at HSE level (Figure S7e and S7f). Moreover, although their band gap values are much widened by HSE (1.30 vs 2.93 eV for spin-up direction at P state, and 1.75 vs 3.27 eV for spin-up channel at AP

state), their energy levels are still in the relative positions as the PBE calculation does. More specifically, the spin-up and spin-down band alignments both belong to type-II for P state, and the spin-up and spin-down channels possess type-I and type-II band alignments for AP state for both cases, respectively. Moreover, the optical properties based on PBE calculations (Figure S7c and S7d) are also similar with those at the HSE level (Figure S7g and S7h). Therefore, all the conclusions drawn at PBE level should be solid.

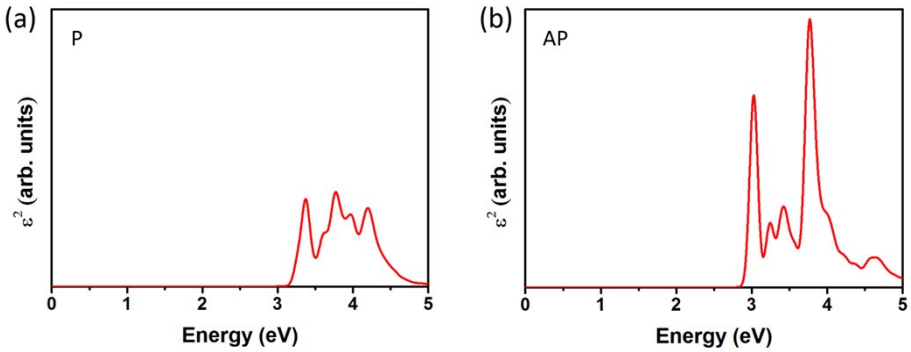

Figure S8. Imaginary part of the dielectric constant of $CrBr_3/CrCl_3$ heterostructure with the electron-hole interaction for (a) P and (b) AP states at GW+BSE levels, respectively.

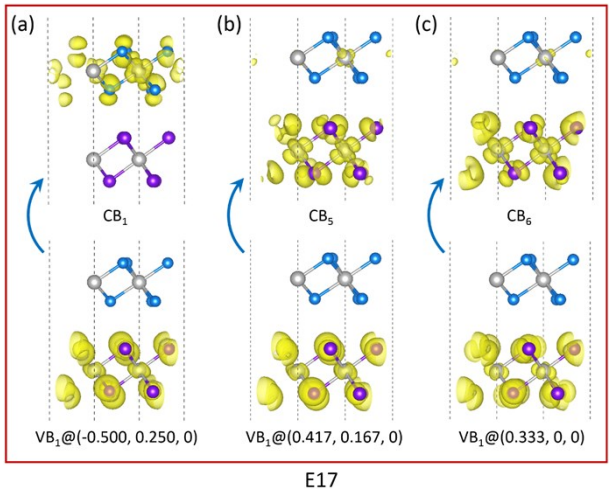

Figure S9. Charge densities of the band-edge states for $CrBr_3/CrCl_3$ heterostructure at specific K points for P state. The blue arrows represent transfer processes. The isosurface value is set as 0.0015 e/Å^3. VB_1, CB_1, CB_5 and CB_6 represent the first valance band, the first, fifth and sixth conduction bands, respectively.

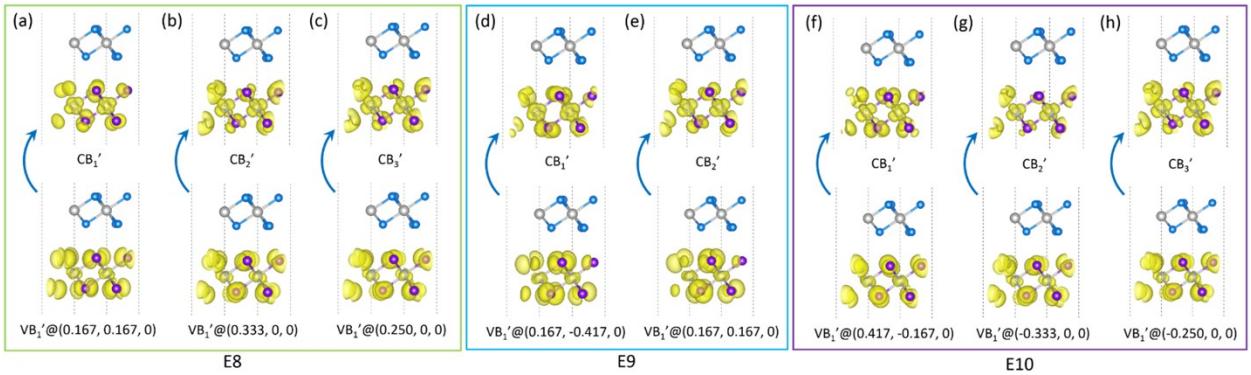

Figure S10. Charge densities of the band-edge states for $CrBr_3/CrCl_3$ heterostructure at specific K points for AP state. The blue arrows represent transfer processes. The isosurface value is set as 0.0015 e/Å^3. VB_1', CB_1', CB_2' and CB_3' represent the first valance band, the first, second and third conduction bands, respectively.

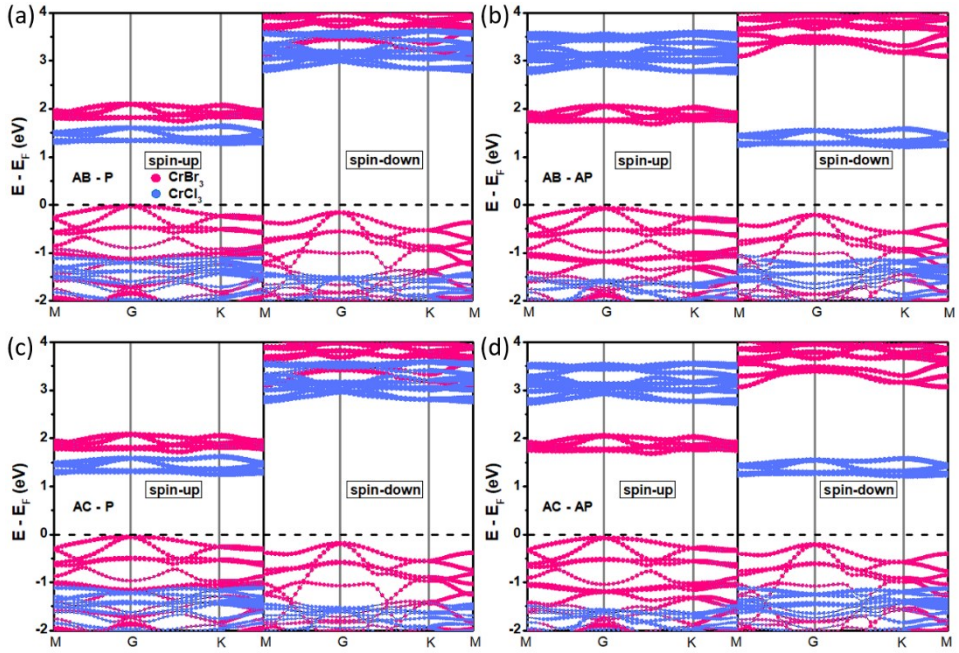

Figure S11. **Band structures of $CrBr_3/CrCl_3$ heterostructure.** (a) and (b) correspond to P and AP states in AB stacking, respectively. (c) and (d) correspond to P and AP states in AC stacking, respectively. Fermi level is set to 0.

The spin-up and spin-down bands both belong to type-II for P state, without obvious orbital hybridization (Figure S11a). The lowest photo-excited spin-up electrons of $CrBr_3$ layer from the valence band to conduction band will then transfer to the lower spin-up conduction band of $CrCl_3$ layer, inducing the separation of electrons and holes and thus producing the photocurrent. When the magnetization direction of $CrBr_3/CrCl_3$ heterostructure is flipped into AP state by the external magnetic field, the spin-up and spin-down channels possess type-I and type-II band alignment, respectively, as shown in Figure S8b. In principle, the light absorption and the quick recombination of electron and hole will occur in $CrBr_3$ layer in spin-up channel, inhibiting the large signal of photocurrent. Additionally, the band structure of metastable state AC-stacking is calculated as well

(Figure S11c and S11d), which is similar to that of AB-stacking. Thereby, the influence of different stacking forms on band alignment can be neglected.

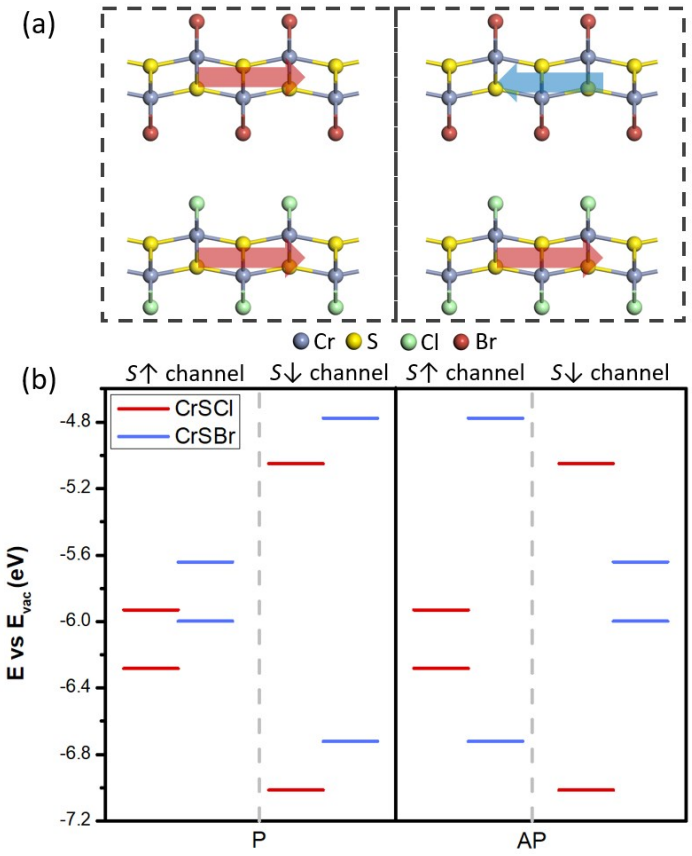

Figure S12. (a) Structures and (b) band edges position relative to the vacuum level of CrSCl/CrSBr heterostructure at P and AP state, respectively.

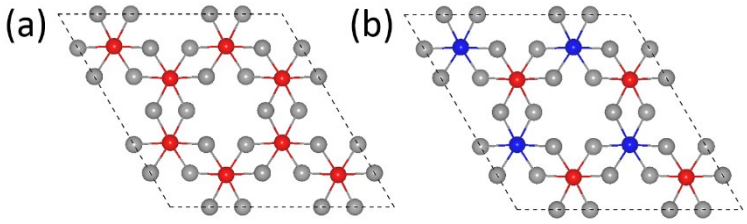

Figure S13. **Top view of spin ordering for CrX_3.** (a) FM and (b) Néel-AFM configuration. Red and blue balls represent spin-up and spin-down magnetic atoms, respectively.

References and Notes

1. B. Huang, G. Clark, E. Navarro-Moratalla, D. R. Klein, R. Cheng, K. L. Seyler, D. Zhong, E. Schmidgall, M. A. McGuire, D. H. Cobden, W. Yao, D. Xiao, P. Jarillo-Herrero and X. Xu, Layer-dependent ferromagnetism in a van der Waals crystal down to the monolayer limit. *Nature,* 2017, **546**, 270-273.

2. Y. Guo, Y. Zhang, S. Yuan, B. Wang and J. Wang, Chromium sulfide halide monolayers: intrinsic ferromagnetic semiconductors with large spin polarization and high carrier mobility. *Nanoscale,* 2018, **10**, 18036-18042.

3. C. Gong, L. Li, Z. Li, H. Ji, A. Stern, Y. Xia, T. Cao, W. Bao, C. Wang, Y. Wang, Z. Q. Qiu, R. J. Cava, S. G. Louie, J. Xia and X. Zhang, Discovery of intrinsic ferromagnetism in two-dimensional van der Waals crystals. *Nature,* 2017, **546**, 265-269.
4. T. Li, S. Jiang, N. Sivadas, Z. Wang, Y. Xu, D. Weber, J. E. Goldberger, K. Watanabe, T. Taniguchi, C. J. Fennie, K. Fai Mak and J. Shan, Pressure-controlled interlayer magnetism in atomically thin CrI3. *Nat. Mater.,* 2019, **18**, 1303-1308.
5. N. Ubrig, Z. Wang, J. Teyssier, T. Taniguchi, K. Watanabe, E. Giannini, A. F. Morpurgo and M. Gibertini, Low-temperature monoclinic layer stacking in atomically thin CrI3 crystals. *2D Mater.,* 2020, **7**.
6. M. A. McGuire, G. Clark, S. Kc, W. M. Chance, G. E. Jellison, V. R. Cooper, X. Xu and B. C. Sales, Magnetic behavior and spin-lattice coupling in cleavable van der Waals layered $CrCl_3$ crystals. *Phys. Rev. Materials,* 2017, **1**, 014001.